REPORT DOCUMENTATION PAGE

Public reporting burden for this collection of information is estimated to average 1 hour per response, including the time for reviewing instructions, searching existing data sources, gathering and maintaining the data needed, and completing and reviewing this collection of information. Send comments regarding this burden estimate or any other aspect of this collection of information, including suggestions for reducing this burden to Department of Defense, Washington Headquarters Services, Directorate for Information Operations and Reports (0704-0188), 1215 Jefferson Davis Highway, Suite 1204, Arlington, VA 22202-4302. Respondents should be aware that notwithstanding any other provision of law, no person shall be subject to any penalty for failing to comply with a collection of information if it does not display a currently valid OMB control number. **PLEASE DO NOT RETURN YOUR FORM TO THE ABOVE ADDRESS.**

1. REPORT DATE *(DD-MM-YYYY)*	2. REPORT TYPE Technical Paper	3. DATES COVERED *(From - To)*

4. TITLE AND SUBTITLE

5a. CONTRACT NUMBER

5b. GRANT NUMBER

5c. PROGRAM ELEMENT NUMBER
62500F

6. AUTHOR(S)

5d. PROJECT NUMBER
2308

5e. TASK NUMBER
M4S7

5f. WORK UNIT NUMBER
345382

7. PERFORMING ORGANIZATION NAME(S) AND ADDRESS(ES)

8. PERFORMING ORGANIZATION REPORT

9. SPONSORING / MONITORING AGENCY NAME(S) AND ADDRESS(ES)

Air Force Research Laboratory (AFMC)
AFRL/PRS
5 Pollux Drive.
Edwards AFB CA 93524-7048

10. SPONSOR/MONITOR'S ACRONYM(S)

11. SPONSOR/MONITOR'S NUMBER(S)

12. DISTRIBUTION / AVAILABILITY STATEMENT

Approved for public release; distribution unlimited.

13. SUPPLEMENTARY NOTES
See attached 13 papers, all with the information on this page.

14. ABSTRACT

15. SUBJECT TERMS

16. SECURITY CLASSIFICATION OF:			17. LIMITATION OF ABSTRACT	18. NUMBER OF PAGES	19a. NAME OF RESPONSIBLE PERSON Kenette Gfeller
a. REPORT Unclassified	**b. ABSTRACT** Unclassified	**c. THIS PAGE** Unclassified	A		**19b. TELEPHONE NUMBER** *(include area code)* (661) 275-5016

AIAA 96-2703

**Plasma and Cathode Emission from a
High Power Hydrogen Arcjet Thruster**

Darren H. Berns, P. Victor Storm, William
A. Hargus, Jr., and Mark A. Cappelli

High Temperature Gasdynamics Laboratory
Department of Mechanical Engineering
Stanford University
Stanford, California

K.A. McFall and R.A. Spores

Propulsion Directorate
OL-AC Phillips Laboratory
Edwards Air Force Base, California

32nd AIAA/ASME/SAE/ASEE
Joint Propulsion Conference
July 1-3, 1996 / Lake Buena Vista, FL

Plasma and Cathode Emission from a High Power Hydrogen Arcjet

D.H. Berns[†], P.V. Storm[†], W.A. Hargus, Jr.[†], M.A. Cappelli[∞]
Department of Mechanical Engineering
Stanford University
Stanford, California

K.A.McFall[**], R.A.Spores[**]
Propulsion Directorate
OL-AC Phillips Laboratory
Edwards Air Force Base, California

Abstract

An experimental study of the measurement of cathode temperature, current distribution, and near-cathode electron number density in a high power hydrogen arcjet is presented. This study is motivated by the desire to better understand arc-electrode interactions in arcjet thrusters, which in many cases, is the main determinate of arcjet lifetime. Measurements such as these may also provide the needed boundary conditions for numerical arcjet simulations, presently under development. We describe in this paper the application of a non-intrusive in-situ measurement technique for on-axis, spectral imaging of the electrode region of arcjets, and the application of this technique to the measurement of the cathode and anode temperatures, cathode spot size, and current distribution in a 30kW hydrogen arcjet thruster. A relatively large field of view (twice the throat diameter) and high spatial resolution (9 µm) are achieved. We find that the maximum cathode temperatures are at or near the melting point of tungsten. We also find that field-enhancement of the thermionic emission process is necessary in order to account for the overall current balance at the cathode. The electric fields extracted are reasonable, given the relatively low plasma conductivity that is estimated on the basis of an LTE and space-charge limited current flow. The current density profiles are sensitive to mass flow rate and arcjet power. In addition to the cathode imaging studies, we have employed axial plasma emission spectroscopy to measure the near-cathode electron number density. The properties estimated from these measurements are used as limits in a model for the cathode current contraction zone.

I. Introduction

The performance of arc discharges as arcjet thrusters for satellite propulsion depends on several key factors, of which electrode erosion and arc-electrode interaction are important. The present use of arcjets for satellite propulsion has expanded the operating realm of these devices and has increased the desire for further understanding of the electrode erosion processes and plasma-electrode interaction. In arcjet thrusters, the measurement of electrode temperatures and the study of arc attachment is often difficult due to the fact that these electrode surfaces are seemingly inaccessible, and that the plasma arc itself is a likely source of optical interference.

Previous studies of arc attachment in prototype arcjets designed for space propulsion have focused primarily on the anode region [1-4]. In these studies, it was learned that the arc anode-attachment can either be diffuse (when the attachment is downstream of the nozzle throat in a low pressure region), or constricted (when the attachment is upstream of the nozzle throat in the high pressure region). Imaging of an exposed cathode in a flowing low pressure plasma has been reported [5]. Although these measurements were not performed on an arcjet, they provided valuable information on arcjet erosion mechanisms, when combined with a model of the near-cathode plasma and conduction within the electrode.

Recently Hoskins et al. applied an optical imaging strategy to measure the anode temperature distribution in regeneratively-cooled arcjets [6]. Although quantitative temperature data is difficult to extract because of the re-radiation of cathode and plasma emission from the observed

---

1

20050815 026

anode surfaces, the results were qualitatively useful in understanding the performance improvements that can be gained by regenerative-cooling. We have previously reported measurements of cathode temperature and current density distribution in low power hydrogen arcjet thrusters [7]. We showed that field-enhanced thermionic emission was necessary to account for the discharge currents used. Field strengths in excess of 10^8 V/m were inferred from these past measurements. Cathode properties have been measured in high current discharges [8], however, as far as we know, no previous direct measurements of cathode properties in high power arcjets have been reported.

Axial and radial spectroscopic plasma emission measurements have been presented previously for both low and medium power arcjets [9-12]. It was shown that the Stark broadened emission in the distant spectral linewings of the H_α transition originates from the hottest, near-cathode regions of these arcjets. From these measurements various parameters were calculated including cathode temperature and electron number densities within the arcjet.

In this paper, we present the results of spectroscopic emission studies implemented to image cathode temperatures and to measure the near-cathode plasma densities. The purpose of the work presented herein was to better understand the near-electrode regions of arcjets, and the differences that may exist between the arc-physics in low and high power arcjets. In addition, these measurements can provide the cathode current density and cathode temperature boundary conditions often imposed in detailed arcjet models. The imaging strategy described here is flexible and can be used with any size of arcjet or arcjet-type of device. This method allows the measurement of the anode throat temperature which has not been done with axial emission measurements. The anode throat size can also be inferred from the images. This allows a monitoring technique for throat closure, which can be an operating limitation in the smaller geometry, higher specific power arcjets of the present.

II. Experimental Setup

Arcjet and Vacuum Facility

An overview of the experimental setups for the axial cathode imaging and the axial plasma emission studies are shown in Fig. 1 and a

schematic of the high power arcjet thruster investigated is shown in Fig. 2. The arcjet was operated in a 2.5 m diameter steel vacuum chamber maintained at a typical background pressure of 80 mtorr during thruster operation by mechanical roughing pumps backing 11,000 l/s blowers. The arcjet was designed and built at Phillips lab and was previously tested using ammonia as a propellant [13]. The arcjet nozzle had a designed throat diameter of 2.54 mm with an 19 degree half angle divergence section leading to an exit diameter of 25.4 mm (100 area ratio). The arcjet cathode was machined from a 3/8" diameter thoriated tungsten rod with a conical tip at a 30 degree half angle. The cathode was set back approximately 4.5 mm from contact with the anode/nozzle constrictor.

Cathode and Anode Imaging

In order to directly study the cathode and anode throat region of the arcjet, a high-resolution (12 μm per pixel - 384 x 578 pixel area) CCD camera coupled to a long distance microscope was used to view the internal surfaces of the arcjet during operation (see Fig. 1a). Optical access to the arcjet was acquired through a 1.5" diameter window downstream of the exit plane in the vacuum facility side flange. The end-on view of the arcjet provided optical access to the cathode tip and a portion of the diverging side of the anode/nozzle. The CCD camera and the long distance microscope were the major components of this cathode/anode imaging system. The long distance microscope is a Questar Corporation, Model DR1 magnifying device. The device has a focal range of 36" to 96" with magnification of 17x (at 36") and 7x (at 96"). The advantage of this device for this application was its large field width, 10mm (at 36") and 23mm (at 96"). With other lenses and attachments the magnification could be increased. The CCD camera used is a Model # TE/CCD-576/UV, temperature controlled device manufactured by Princeton Instruments Inc. The camera has 14 bit A/D conversion, exposure times of 5ms-23 hours, a readout rate with 100kHz capability, and a shutter time of 5-6ms. Based on our previous studies of cathode emission in low power arcjets [7], we found that for wavelengths greater than 700 nm, the intensity of axial emission is dominated by thermal emission from the cathode, and there is little or no interference from the luminous plasma. Therefore, a 700nm, 10 nm bandwidth, and an 810nm, 10 nm bandwidth interference filter were chosen such that the cathode emission could be

isolated from the hydrogen lines and the continuum emission due to free electrons in the plasma.

Light emitted from the arcjet was collected by the long distance microscope through a series of redirecting mirrors. The long distance microscope was adjusted such that the focal plane was at the cathode surface of the arcjet. The light exiting the long distance microscope was then focused onto the photo-sensitive array in the CCD camera. For a given arcjet operating level, the appropriate exposure time (controlled by the camera shutter speed) was chosen such that the array was not saturated but a significant signal was obtained. The image was converted to a set of digital signals (one value for each pixel of the array) within the detector/controller and the signals were then stored on a P.C. for post-processing. Images were acquired for several specific power levels (input power/propellant flow rate). Intensity calibration was performed with a tungsten filament lamp, placed at the position of the arcjet, the temperature of which was determined by a single color Minolta Cyclops 152 optical pyrometer, accounting for the temperature-dependent spectral emissivity [14].

Separate images were taken of the cathode region with both filters for several different arcjet operating conditions. This data was used to calculate all of the cathode properties presented in this paper. At each operating level, the cathode shutter speed was adjusted so that the radiation emitting from the cathode tip could be captured without saturating the CCD array. The images capture the cathode tip, the anode throat, and between radii of 0.3 mm to 2.3 mm of the diverging section of the anode, depending on the orientation of the camera.

Axial Plasma Emission Studies

The axial plasma emission was measured and analyzed in a manner similar to previous studies performed on 1-kW and 5-kW arcjets [9,10]. The experimental setup is shown in Fig. 1b. A 400 mm focal length achromat lens was used to collect light axially from the arcjet throat and bring it to a focus on a 50 μm diameter spatial filter. The image at the spatial filter was then focused, using an 100 mm focal length achromat lens, onto the entrance slit of an Acton Research Corp. (model SpectraPro 500) 0.5 m monochromator containing a 2400 gr/mm grating. The entrance and exit slits of the monochromator were each set to 5 μm, yielding a

spectral resolution of 0.004 nm. A Hamamatsu R928 photomultiplier tube was used as the photodetector. Phase-sensitive detection was performed for background noise rejection using a Stanford Research Systems SR850 digital lock-in amplifier. The reference signal was provided by a mechanical beam chopper placed near the intermediate focus at the spatial filter and set at a chopping rate of 1 kHz. The digitized output of the lock-in amplifier was transferred to a personal computer for spectral analysis. To minimize the light collection volume from the arcjet plume and hence reduce the possibility of collecting molecular hydrogen emission, an aperture stop of 11 mm diameter was placed in front of the collection lens, providing a collection optics f/# of approximately 150. The image magnification at the spatial filter was approximately 0.3 which provided a resulting spatial resolution at the arcjet constrictor of approximately 160 μm. As with the cathode imaging experiments, intensity calibration was performed using an 18 A tungsten filament lamp placed at the location of the arcjet, and the temperature of the lamp was determined by optical pyrometry.

Axial emission scans of the hydrogen Balmer-alpha (Hα) line were taken at four different operating conditions and several radial positions across the constrictor diameter. Three of the operating conditions were at a mass flow rate of 123.5 mg/s, the same flow rate used in part of the cathode imaging study, while the fourth condition was at a lower flow rate (82.0 mg/s). The scans were performed in a period of 2 minutes and data was sampled at 8 Hz, resulting in 960 data points per scan. The recorded lineshapes were analyzed to determine electron number density in the arc region near the cathode as explained in the results section below. In addition to the Hα scans, the axial emission over the complete visible spectrum (400-700 nm) was collected, in 5 minute scans, on the arcjet centerline at three different operating conditions in an attempt to determine the cathode temperature from the spectral distribution of the cathode emission.

III. Results

Spectral axial plasma emission scans of the arcjet are shown in Fig. 3 for the wavelength range between 400 nm and 700 nm. Previous axial plasma emission measurements performed on a medium-power hydrogen arcjet [10] revealed that the hydrogen Balmer-series line emission dominates

most of the visible spectrum. However, unlike these prior studies, we find here that the continuum emission between the H_α and H_β spectral lines was greater than that which can be accounted for by cathode emission and free-free or free-bound transitions alone, and speculate that the source of this emission may be electronically excited molecular hydrogen. It is evident from Fig. 3 that in the spectral region beyond the H_α line, the continuum emission intensity falls dramatically. Beyond approximately 700nm, the cathode thermal emission is assumed to dominate in the emission. As a result, we selected 700 nm and 810 nm as candidate wavelengths for electrode imaging. Although longer wavelengths may further reduce the contributions from interfering emission, wavelengths beyond 810 nm were not selected due to the loss of sensitivity in the CCD camera. Also, at 3900 K the peak of the back-body emission is located at 743 nm, therefore, going farther into the infrared would reduce the signal from the cathode emission.

In addition to direct observation of the cathode, the field of view of the long distance microscope also provided for imaging of a large fraction of the anode in the region of the nozzle throat. Thermal emission from the anode surface very near the throat is expected to be only weakly affected by re-radiation of plasma and cathode emission from other regions of the anode.

The cathode images were obtained during arc operation by acquiring the continuous radiation emitted from the high temperature cathode tip and the throat region of the anode. From these images, the cathode radial temperature distribution could be measured. The cathode temperature was calculated from comparison of the cathode tip local radiation, again for various arcjet operation levels, with calibrated data obtained from a tungsten arc lamp. Given the temperature distribution, other properties were determined such as the current density distribution along the cathode, the cathode spot size, and the electric field in front of the cathode. The cathode spot diameters were inferred from the current density profiles. Due to the Gaussian shape of the current density profile, measurement of the halfwidth of the profile (position of greatest slope) provides a good estimate for the cathode spot diameter. The spot diameters calculated with this method range from 0.5 to 0.75 mm.

From the calibration procedure, the CCD signal was converted to graybody intensity ($W/m^3/Sr$):

$$I_\lambda(\lambda,T) = \varepsilon_\lambda I_{\lambda,b}(\lambda,T) = \frac{2hc_o{}^2\varepsilon_\lambda}{\lambda^5\left[exp\left(\dfrac{hc_o}{\lambda kT} - 1\right)\right]} \quad (1)$$

Here, $I_{\lambda,b}$ is the Planck distribution, relating the wavelength (λ) dependent intensity of an ideal blackbody to the object temperature, T. The constants h, k, and c_o refer to Planck's constant, Boltzmann's constant, and the speed of light in vacuum, respectively. We believe the largest source of error to be in the selection of the spectral emissivity, ε_λ, at the wavelength of interest. The spectral emissivity of tungsten at or above the melting point has not been previously measured. For the calculations described here, we have used a value of 0.4 [14].

Fig. 4 is a typical intensity image acquired by viewing the arcjet electrode region during operation. The left and right figures are the same image but with different intensity threshold settings to illustrate all of the features of the electrode region. The figures show the entire throat of the arcjet, the portion of the cathode visible through the throat, and a portion of the diverging section of the anode. The left figure shows the varying levels of intensity across the cathode, with a label tagged to the center of the cathode. The right figure identifies the throat region. The two sides of the throat along the cross-section are labeled "A" and "B" for reference. It is clear from these images that the cathode was misaligned in this arcjet. This misalignment causes asymmetric temperature and current density profiles. The bright spots on the diverging section of the anode are believed to be previously melted droplets of tungsten (the origin of which is unclear) that have resolidified. The most remarkable finding from this study is that the identification of the cathode and throat are quite clear, along with features such as these droplets, despite the fact that we are observing these internal surfaces through an intense arc that is probably heated to temperatures above 15,000K. The cathode temperature profile is taken along a vertical cross-section through the image, denoted by the dashed line. All of the profiles presented in this paper are taken from this same orientation. The top of the figure is referenced as the negative position side in the temperature and current density profiles.

4

Fig. 5 shows the measured temperature profiles obtained from images of the electrode region of the arcjet for three different operating conditions. The profiles are cross-sections through the nozzle. The centerline (r=0) is a local center, determined by choosing the location of the peak temperature, and does not necessarily correspond to the exact geometric center of the cathode tip or the constrictor. This choice of r=0 is the method used for all figures. The uncertainties in temperature have been estimated to be approximately ± 220 K near the cathode (from centerline out to a radius of about 0.3 mm) and ± 180 K in the anode regions (beyond radius of 0.3 mm). These uncertainties are based on an expected error in the calibration constant of 10%, an error in emissivity of ±0.05, and an error in the signal due to dark noise in the camera.

For operation on hydrogen at a current of 154 A and a flow rate of 123.5 mg/s the cathode peak temperature is 3911 K, the anode temperature ranges from 2700 K on one side of the throat to about 2450 K 3.2 mm away from the throat (axial distance). It can be seen that there is no discernible temperature step at the cathode throat. This implies that the cathode and anode temperatures at this radial point are nearly the same. The temperature decreases as you go out from the throat for a short distance, then increases several hundred degrees, and finally decreases again. The increase coincides with the hot spot on the images, which as previously discussed, appears to be a resolidified droplet of tungsten. The temperature of this droplet appears to be higher than its surroundings. These anode temperature values are probable upper limits to the temperatures since reflections from the interior surface of the nozzle are not taken into account in the calculation of relative intensity at a given radial location. This correction requires knowledge of the angular and temperature dependence of the spectral emissivity.

For the same flowrate, 123.5 mg/s, increasing the current to 210 A causes the temperature profile to widen and increases the temperature values along both the cathode and the anode. The cathode peak temperature is nearly the same at 3965 K. As will be shown by the current density profiles, increasing the current at the same flowrate causes the cathode spot to widen (from 0.64 mm to 0.73 mm) and therefore broadens the temperature profiles. All of the temperature values increase due to the increased energy density at the cathode surface caused by the increased current.

For nearly the same current, 146 A, increasing the mass flow rate causes the temperature profile to narrow and decreases the temperature values along both the cathode and the anode. The cathode peak temperature is again nearly the same at 3954 K. As will be shown by the current density profiles, increasing the flowrate for a fixed current causes the cathode spot to narrow (from 0.64 mm to 0.58 mm) and thereby narrows the temperature profile. All of the temperature values decrease because the energy density in the flow, or the specific power, decreases. An interesting but perhaps not significant finding is that at nearly comparable currents (154A and 146A), increasing the mass flow rate from 123.5 mg/s to 179 mg/s increased the center cathode temperature slightly (while decreasing the spot size). Increasing the mass flow rate appears to constrict the arc, requiring a higher centerline arc temperature to provide the higher electron emission necessary to conduct the same amount of total current through less of an area.

Fig. 6 shows the calculated current density profiles for the temperature profiles shown in Fig. 5. In Fig. 7, we display three current density profiles for the same arcjet operating conditions: (i) the current density for a purely thermionic emitting cathode and a work function equal to that of pure tungsten; (ii) the current density for a field-enhanced (Schottky-enhanced) thermionic cathode using the work function of pure tungsten and a finite (and relatively high value) for the electric field at the surface, and (iii) a curve illustrating that the profile generated in the field-enhanced case could also be obtained using pure thermionic emission if the work function were lowered.

The results of previous studies [15] have suggested that the cathodes in these types of devices emit electrons based on the principle of field-enhanced thermionic emission, where the electric field at the cathode surface acts to reduce the potential barrier at the surface for electron emission. The field-enhanced thermionic emission current density is derived from the equation [16,17]:

$$J_{th} = AT_c^2 \exp\left[\frac{-e}{kT_c}\left(\phi_w - \left(\frac{eE_s}{4\pi\varepsilon_o}\right)^{1/2}\right)\right] \qquad (2)$$

where T_c is the local cathode temperature, ϕ_w is the work function of the cathode (4.5 V for pure tungsten [18]), E_s is the electric field strength at the surface of the cathode, and A is a constant

equal to 1.202×10^6 A/m^2/K^2. Purely thermionic emission is governed by the same equation with $E_s=0$. Previous experiments showed that the thorium in the cathode migrates out of the cathode tip and after short operation times the cathode tip is left with virtually no detectable thorium [15]. This cathode had been run extensively, therefore, it was expected that the cathode tip was pure tungsten.

Based on the measured temperature distributions it is possible to calculate the current density at each radial location where there is a temperature value. The integral of current density times the differential area gives the total enclosed current. In this calculation, the electric field is changed iteratively until the total enclosed current matches the measured current of the arcjet.

For the arcjet operating conditions of 123.5 mg/s and 154 A, it was necessary to use an electric field of 5.45×10^8 V/m in order to reproduce the total enclosed current (see Fig. 7). In the absence of field-enhanced emission, a pure tungsten cathode with the measured temperature distribution would emit a total current of 8.85 A, far below the actual measured current. Note that the measured total current density of 154 A could be obtained with pure thermionic emission if the work function were lowered to 3.61 V.

A comparison of the current density profiles in Fig. 6 illustrates the dependence of cathode arc attachment on current and flowrate. For arcjet operating conditions of 123.5 mg/s of hydrogen and 154 A, the peak current density is 4×10^8 A/m^2. The uncertainty in current density at the centerline is estimated to be approximately 1×10^8 A/m^2. This uncertainty is based on an expected error in the work function of ± 0.1 V and the expected error in temperature of ± 220 K. For the same flow rate, increasing the current to 210 A, causes the current density profile to widen and the values at all radial positions to increase, with a peak of 5.1×10^8 A/m^2. The calculated electric field of 5.77×10^8 V/m is nearly the same as for the 154 A case. As discussed within the context of the measured temperature, the cathode spot diameter increases. It is expected that this coincides with a broadening of the arc column diameter with increased current.

For nearly the same current (146A), increasing the mass flow rate causes the current density profile to become more narrow, while increasing the peak value to 5×10^8 A/m^2. This is consistent with the interpretation of the temperature profiles, i.e., for a narrower profile the peak must increase in order to have the same total current

(area under the profile). The narrower profile corresponds to a smaller diameter cathode spot. This is attributed to a narrower arc column. For the same current, when the flowrate is increased there is an increase in the convective heat transfer from the arc causing the arc to constrict to smaller diameters and causing a corresponding increase in the arc temperature, a necessary response so that there is an increase in the electrical conductivity.

Previous studies of the axial emission from 1-kW and 5-kW arcjets have demonstrated that the arc electron number densities in the near-cathode region can be determined from an analysis of the atomic hydrogen H_α line [9,10]. This is accomplished by fitting a Lorentzian line to the linewings only, since the line center is strongly affected by radiative transfer in the nozzle expansion region and in the plasma plume [9]. The FWHM of the best fit Lorentzian is a direct measure of the electron number density in the arc by the Stark broadening mechanism. The conditions within the arc, as determined by models of low power arcjets [19], indicate that Stark broadening is the only significant broadening mechanism in the arc region.

Typical scans of the H_α line as a function of radial position at one operating condition (123.5 mg/s and 20 kW) are given in Fig. 8. The dip near the linecenter is due to reabsorption by the cooler, less dense plasma in the nozzle expansion region and in the plasma plume. This dip was predicted by a radiation model for a 1-kW arcjet and was previously seen in the axial emission of 1-kW and 5-kW arcjets [9,10]. The far wings of the lineshape are determined by charged-particle collisional broadening of the line emission in the hot arc region near the cathode. By fitting a Lorentzian lineshape to the far wings of the line, the electron number density was determined from the linewidth, using dynamic-ion Monte-Carlo simulations of the Stark broadening of H_α [20]. The calculated electron number densities are shown as a function of arcjet power and radial position in Figs. 9 and 10. These results indicate that the arc electron number density increases slightly with arcjet power at a constant propellant flow rate. This result was previously observed in a 5-kW arcjet [10] and is consistent with the increase in the arc current with increasing arcjet power. The higher current must be supported by greater current densities in the arc, which requires a greater plasma conductivity, hence, a greater electron number density.

The large uncertainties displayed in Fig. 9 are primarily a result of the sensitivity of the best fit Lorentzian linewidth to the amount of the linewings used in the fitting procedure. This uncertainty constitutes the limiting factor in accurately determining the arc electron number density from the linewings. On the one hand, to ensure that the fit is performed only to the part of the line originating near the cathode, it would be desirable to fit only the very far wings. This will reduce the systematic error associated with the radiation transfer near line center. On the other hand, since the noise is larger in the wings of the line, performing a line fit to only the far wings results in a very large statistical error in the determination of the linewidth. As a consequence the measured near-cathode electron number density has considerable uncertainty. The error bars were intentionally omitted from Fig. 10 to avoid cluttering the figure; however, the uncertainties were similar to those given in Fig. 9.

The complete visible spectrum of the axial emission is shown in Fig. 3 for three operating conditions. The region of the spectrum away from the Balmer series lines constitutes background graybody emission from the cathode surface and plasma emission from sources other than atomic hydrogen, which includes continuum radiation from the electrons and molecular hydrogen emission. An attempt was made to determined the peak cathode temperature from the region of the spectrum between the H_α and H_β lines; however the measured intensities were much greater than that which would be produced by thermal emission from the cathode at a reasonable temperature. This indicates that the background emission in this region of the spectrum is dominated by either continuum electron emission (bremsstrahlung radiation) or molecular hydrogen emission.

IV. Discussion

The measured peak cathode temperatures range from 3900-4000K (±220K). These temperatures are above the melting point of tungsten, suggesting that there may be a highly non-equilibrium process associated with evaporation of tungsten from the surface. The electric fields calculated for the operating conditions in the above cases are on the order of 5.0×10^8 V/m ($\pm 1.0 \times 10^8$ V/m). These electric fields are on the same order of magnitude as values previously reported [7,10,15,21]. It should be noted

that fields in excess of approximately 10^7 V/m start to distort the potential barrier for electron emission at the electrode to the extent that electron tunneling through the barrier becomes significant [22]. This tunneling phenomenon, commonly referred to as field emission, becomes important when the thickness of the barrier approaches the wavelength of the free electrons in the tungsten electrode. In essence, the mechanism for current transfer from cathodes in these arcjets may be more complicated then previously thought [15,21], and a mechanism based simply on field-enhanced thermionic emission may be a simplification of the actual case.

In order to understand the physical significance of such high field strengths inferred from the analysis, we have undertaken a simple analysis based on the assumption of space-charge limited electron current flow. Very near the cathode, we would expect that the plasma conducts the thermionically emitted electron current according to the space-charge limited value:

$$J_e \approx \sigma_{es} E_s \qquad (3)$$

where σ_{es} represents the electrical conductivity of the plasma adjacent to the cathode surface. If we assume a value of $\sigma_{es} = 0.01$ mho/m, which is very near that of an atmospheric pressure plasma in local thermodynamic equilibrium at a temperature of 4000 K [23] (typical of the peak temperatures measured), then the required field needed to conduct an emitted electron current of 150 A near the central cathode region is greater than 5×10^{10} V/m. The measured fields of 10^8 V/m suggest that the plasma conductivity is approximately 100 times that of the equilibrium conductivity. Therefore, the plasma in front of the cathode is expected to be overdense with electrons and ions as compared to Saha equilibrium.

The measured electron density distributions in Fig. 10. indicate that the arc column in the vicinity of the most luminous (highest temperature) region is nearly the diameter of the throat, i.e. 2.5 mm, as inferred from the FWHM of the electron number density profiles. This suggests that the arc contracts at the cathode surface since the diameter of the arc root attachment at the cathode surface, as previously discussed, is approximately 1 mm. This contraction is necessary since the plasma conductivity near the cathode is expected to drop dramatically (the cathode is maintained at a temperature that is considerably lower than the arc). The contraction of an arc at a cathode surface has been modeled previously by Felderman and

McDermott [24] within the framework of a quasi-one-dimensional model for heat conduction from the arc plasma to the cathode. In that study, they introduce the so-called concentration layer thickness, L_C, which defines the distance near the cathode over which the arc contracts. If we assume that the thermal conductivity of the plasma is unchanging over this distance, then an expression for the concentration layer thickness is given in Ref. 24 as:

$$L_c = \frac{\xi}{J_c}\left\{\frac{(T_{arc}-T_c)\sigma_{arc}k_{arc}}{ln\,\xi - 1}\right\}^{1/2} \quad (4)$$

where ξ is the current contraction parameter [24]:

$$\xi = \frac{J_c}{J_{arc}}\left\{\frac{\sigma_{arc}}{\sigma_c}\right\}^{1/2} - 1 \quad (5)$$

Here, J_C and J_{arc} are the average current densities at the cathode surface and in the distant arc respectively; σ_c and σ_{arc} are the plasma electrical conductivities at the cathode surface and in the distant arc, k_{arc} is the thermal conductivity of the arc, and T_{arc} is the average arc temperature. Using a value of $T_{arc} \approx 12,000K$ (which is consistent with what is calculated using the measured electron number densities and a pressure which is close to the pressure upstream of the cathode, assuming full ionization), $J_c = 3.0 \times 10^8$ A/m^2 (approximately the average of the measured current density in Fig. 6), $J_{arc} = 4.8 \times 10^7$ A/m^2 (calculated from the typical operating current of 150 A and the arc diameter estimated from Fig. 10 of 2 mm), $\sigma_{arc} = 4 \times 10^3$ mho/m at the arc temperature [23], $\sigma_c = 2$ mho/m (from the measured current density and electric field at the cathode), and an arc conductivity $k_{arc} = 5.5$ W/m/K [23], we arrive at: $\xi = 280$ and $L_c = 5.7$ mm.

It appears therefore that within the framework of the quasi-1D model, the arc in the constrictor contracts to the diameter of the cathode spot over a distance greater than the sum of the setback distance of the cathode from the constrictor and the constrictor length. The result of this simple analysis and the expectation of a strong radial conduction loss near or within the constrictor indicates that in an arcjet thruster the arc attachment and contraction at the cathode is a strongly two-dimensional phenomenon, and any analysis of the cathode region must be based on a two-dimensional analysis of heat conduction.

V. Summary

We have presented an experimental study of the measurement of cathode temperature, current distribution, and near-cathode electron number density in a high power hydrogen arcjet. The cathode temperature and current distribution measurements are based on a non-intrusive, in-situ technique for on-axis spectral imaging of the electrode region. A relatively large field of view (twice the throat diameter) and high spatial resolution (9 μm) are achieved. We find that the maximum cathode temperatures are in the range of 3800-4000K. We also find that field-enhancement of the thermionic emission process is necessary in order to account for the overall current balance at the cathode. The electric fields extracted are typically 5x10^8 V/m, a reasonable magnitude given the relatively low plasma conductivity that is estimated on the basis of LTE and space-charge limited current flow. The maximum current densities are typically 4x10^8 A/m^2 to 5x10^8 A/m^2 and the profiles are found to be sensitive to mass flow rate and arcjet power. As expected, the current density profiles constrict in size when the mass flow rate is increased for a constant current and expand in size as the current is increased for a constant mass flowrate. In addition to the cathode imaging studies we have employed axial plasma emission spectroscopy to measure the near-cathode electron number density and its variation with radial position. The properties estimated from these measurements are used as limits in a quasi 1-D model for the cathode current contraction zone. It is deduced that the contraction of the arc at the cathode is a strongly two-dimensional phenomenon and models describing cathode attachment in arcjets must account for two-dimensional effects.

Acknowledgments

References

1. Curran, F.M., et al., "Performance Characterization of a Segmented Anode Arcjet Thruster," AIAA 90-2582, (also NASA TM 103227), July 1990.

2. Curran, F.M. and Manzella, D.H., "The effect of Electrode Configuration on Arcjet Performance," NASA TM 102346, 1989.

8

3.   Sankovic, J.M. and Berns, D.H., "Performance of a Low-Power Subsonic-Arc-Attachment Arcjet Thruster," AIAA 93-1898, June 1993.

4.   Berns, D.H. and Sankovic, J.M., "Investigation of a Subsonic-Arc-Attachment Thruster Using Segmented Anodes," AIAA 93-1899, June 1993.

5.   Zhou, X., Berns, D.H., and Heberlein, J., "Investigation of Arc-Cathode Interaction," AIAA 94-3129, June 1994.

6.   Hoskins, W.A., Butler, G.W., and Kull, A.E., "A Comparison of Regenerative and Conventional Arcjet Performance," AIAA 94-3124, June 1994.

7.   Berns, D.H., Storm, P.V., and Cappelli, M.A., "Spectral Imaging of the Arcjet Electrode Region," AIAA 95-1957, June 1995.

8.   Goodfellow, K.D. and Polk, J.E., "Experimental Verfication of a High-Current Cathode Thermal Model," AIAA 95-3062, July 1995.

9.   Storm, P.V. and Cappelli, M.A., "Axial Emission Diagnostics of a Low Power Hydrogen Arcjet Thruster," IEPC-93-219, September 1993.

10.   Storm, P.V. and Cappelli, M.A., "Axial Emission Measurements on a Medium-Power Hydrogen Arcjet Thruster," AIAA 94-2743, June 1994.

11.   Cappelli, M.A and Storm, P.V.., "Interior Plasma Diagnostics of Arcjet Thrusters," AIAA-94-2654, June 1994.

12.   Ishii, M. and Kuriki, K., "Optical and Analytical Studies of Arc Column in DC Arcjet," AIAA-87-1086, May 1987.

13.   Hargus, W.A., Micci, M., and Spores, R., "Interior Spectroscopic Investigation of the Propellant Energy Modes in an Arcjet Nozzle," AIAA-94-3302, 30th Joint Propulsion Conference, June, 1994.

14.   Larrabee, R.D., J. Optical Society of America, **49**, 619, 1959.

15.   Curran, F.M. and Haag, T.W., "Arcjet Cathode Phenomena," JANNAF Propulsion Meeting, 1989, (also NASA TM 102009).

16.   Koester, J.K., "Analytical and Experimental Studies of Thermionically Emitting Electrodes in Contact with Dense Seeded Plasmas", Ph.D. Thesis, C.I.T., 1970.

17.   Cobine, J.D., Gaseous Conductors, Dover Publications, New York, 1958.

18.   CRC Handbook of Chemistry and Physics, 73rd Ed., CRC Press Inc., Boca Raton, FL, 1992.

19.   Butler, G.W., Kull, A.E., and King, D.Q., " Numerical Simulations of Hydrogen Arcjet Performance," IEPC-93-249, September 1993.

20.   Kelleher, D.E., Wiese, W.L., Helbig, V., Greene, R.L, and Oza, D.H., "Advances in Plasma Broadening of Atomic Hydrogen," *Phys. Scripta*, T47, pp. 75-79, 1993.

21.   Bade, W.L. and Yos, J.M., "Theoretical and Experimental Investigation of Arc Plasma Generation Technology," AVCO Corp., 1962.

22.   Bardeen, J., "Flow of Electrons and Holes in Semiconductors," Handbook of Physics, sect. 8, ch.6, pg. 79, McGraw Hill, 1967.

23.   Boulos, M.I., Fauchais, P., and Pfender, E., Thermal Plasmas, Volume 1, Plenum Press, New York, 1994.

24. Felderman, E.J. and MacDermott, W.N., "Near-electrode Model with Nonequilibrium Ionization (at 100atm)," AIAA-95-1993, 1995.
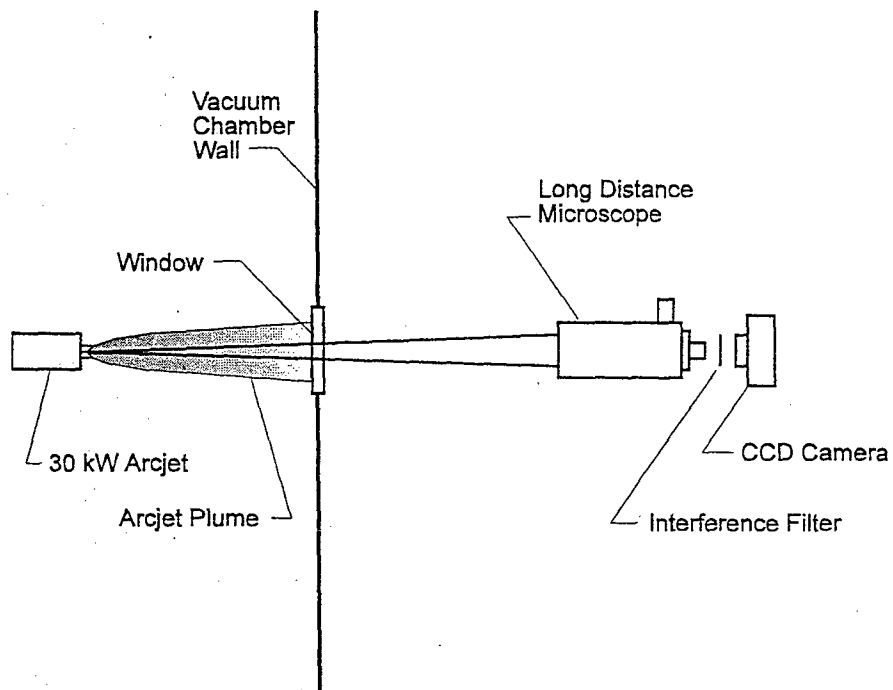
Figure 1a. Experimental setup for the cathode imaging study.
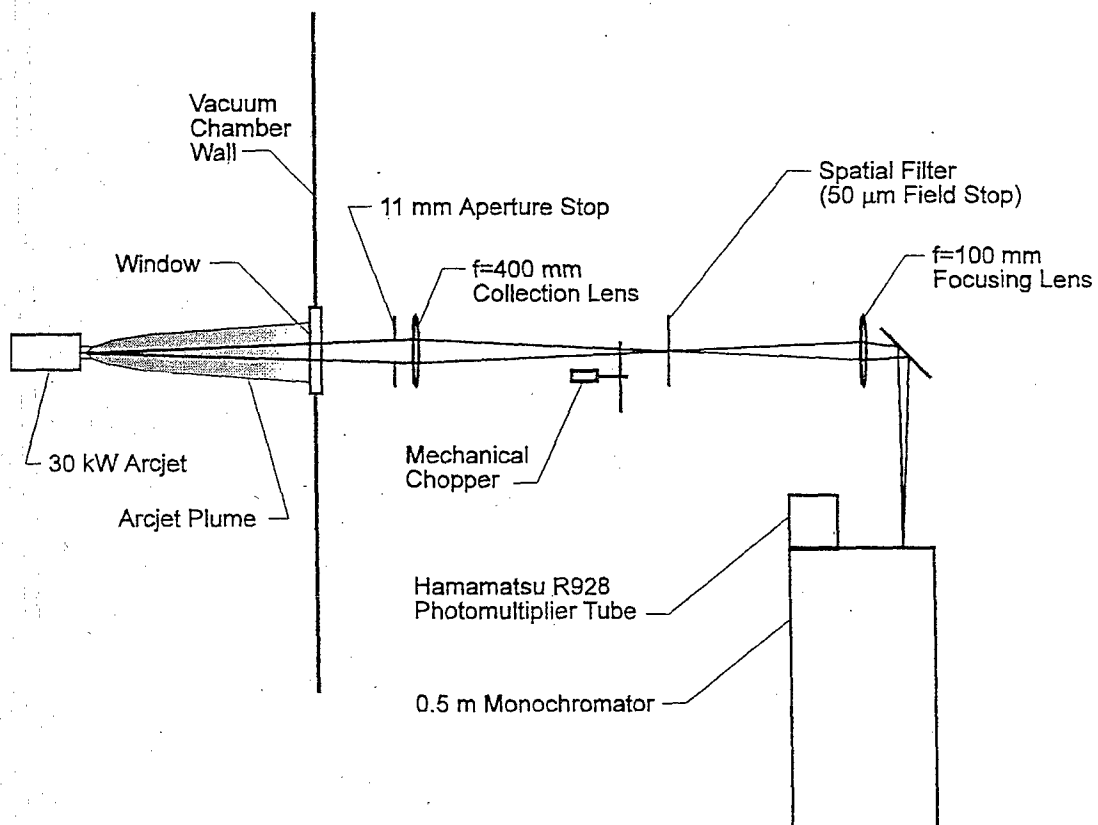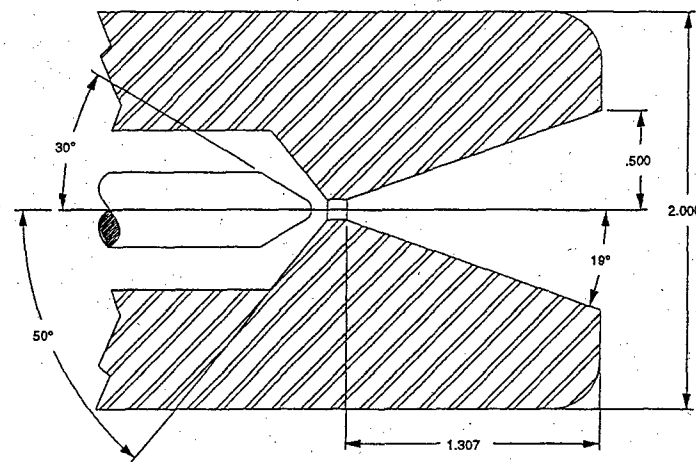

Figure 1b. Experimental setup for the axial emission study.

all dimensions in inches

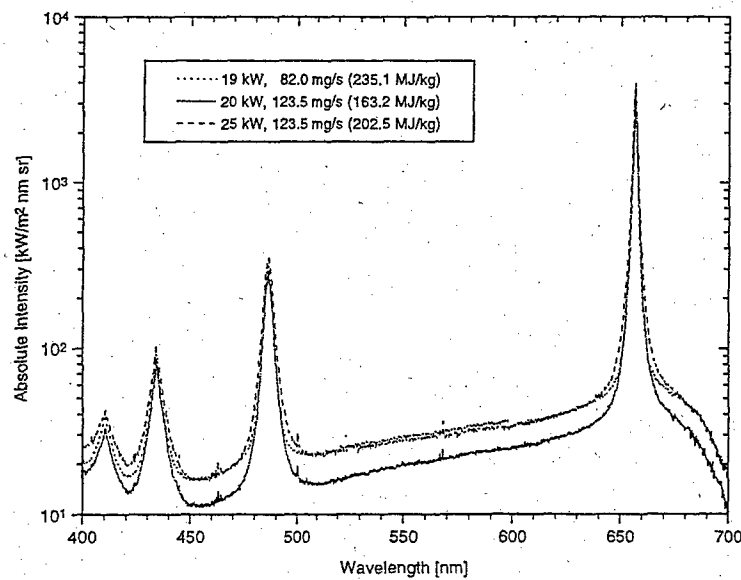Figure 2. High Power Arcjet Electrode Region

Figure 3. Calibrated axial emission intensity over the complete visible spectrum.
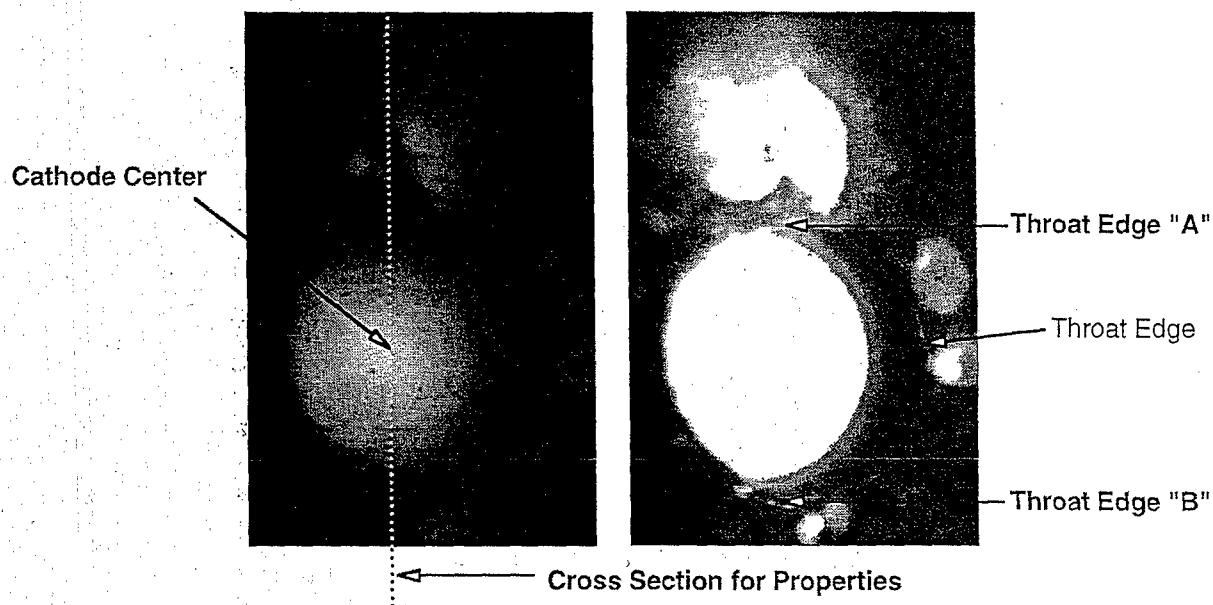
Figure 4. Typical electrode image taken during arcjet operation. Left and right are the same image with different intensity threshold
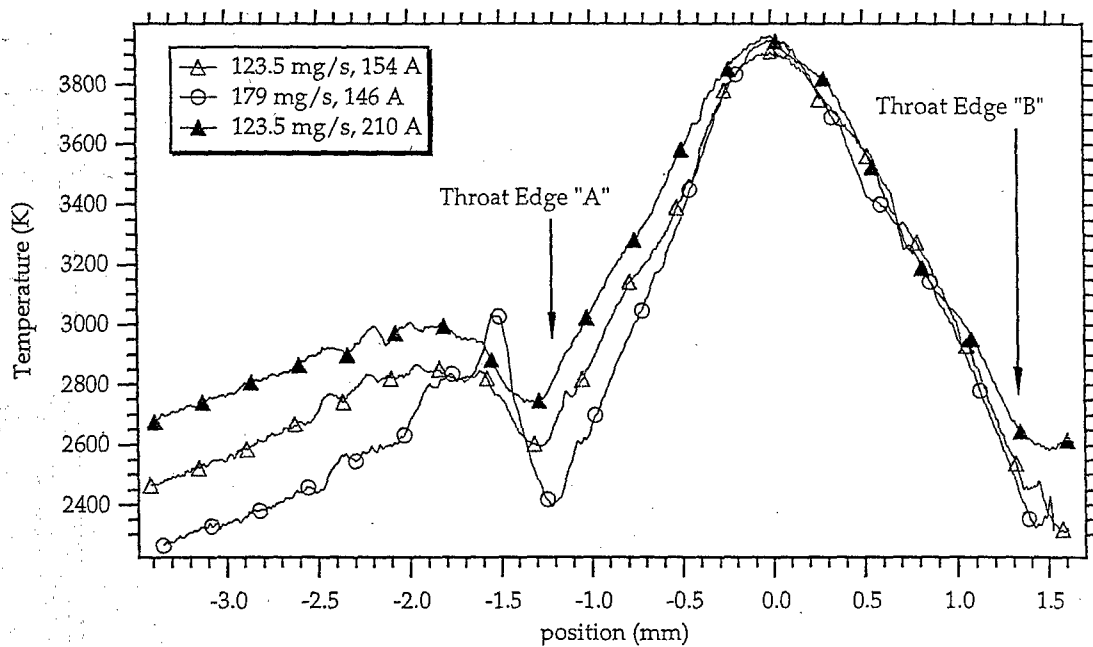

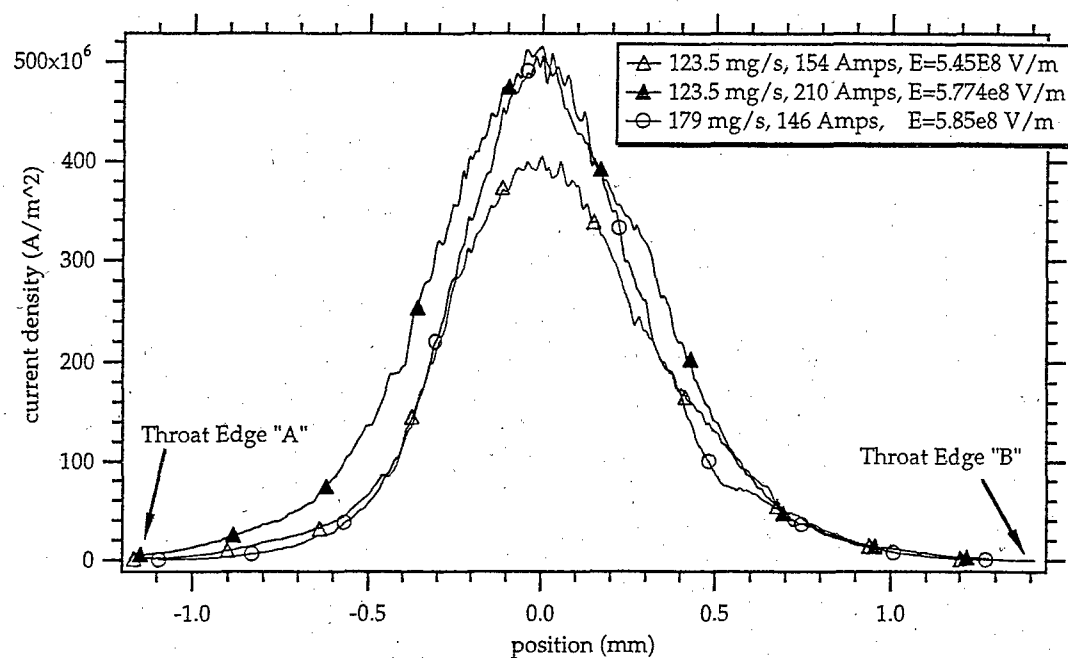Figure 5. Arcjet electrode temperature as a function of radial location

Figure 6. Current density as a function of radial location
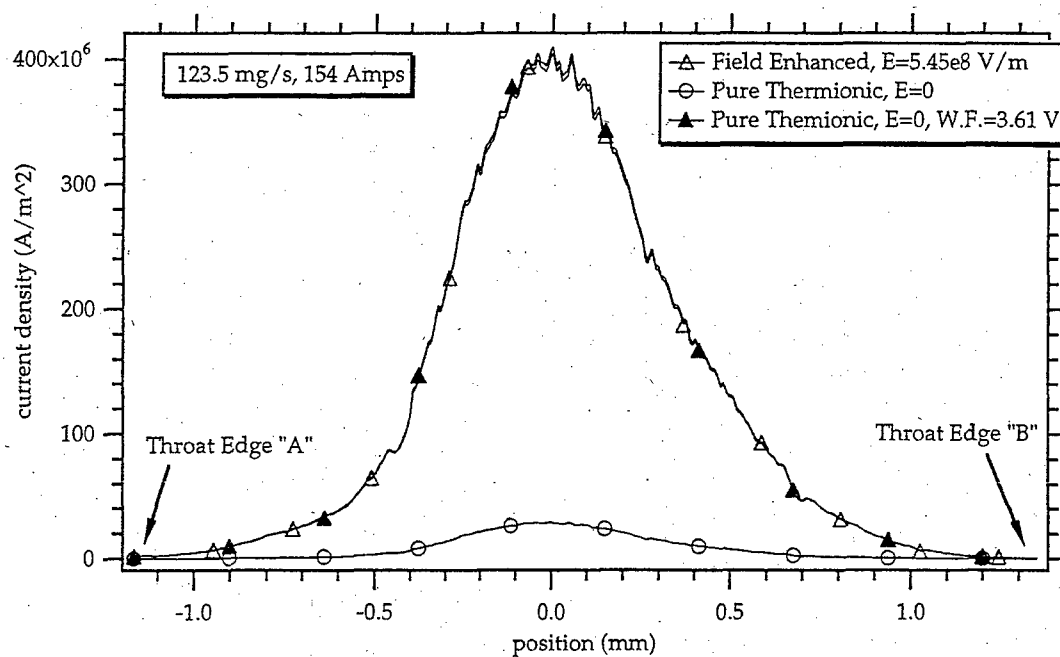
Figure 7. Pure thermionic emission verses field-enhanced thermionic emission
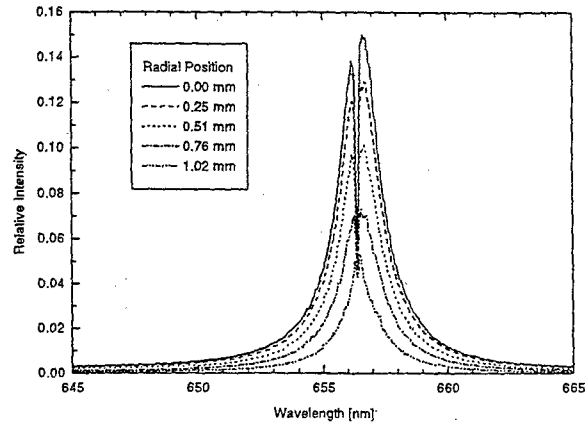as a function of radial location

Figure 8. Uncalibrated H_α lineshapes at various radial positions for the operating condition: 20 kW, 123.5 mg/s (163.2 MJ/kg).
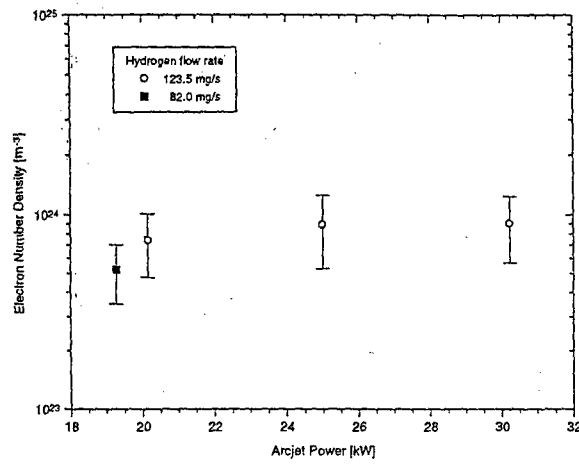

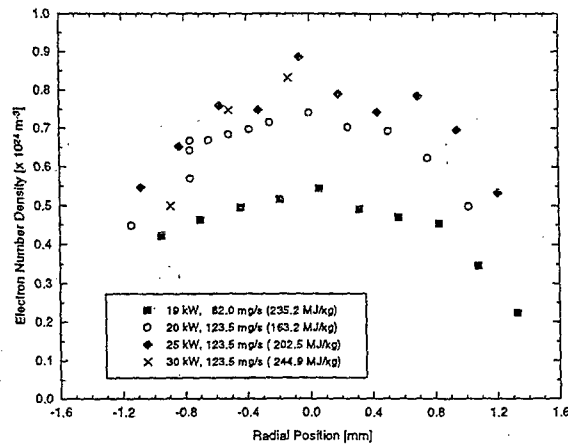Figure 9. Centerline arc electron number density as a function of arcjet power.

Figure 10. Arc electron number density as a function of radial position.